



RESEARCH ARTICLE | JULY 11 2019

Phase field lattice Boltzmann model for air-water two phase flows

E. Dinesh Kumar ; S. A. Sannasiraj ; V. Sundar 



Physics of Fluids 31, 072103 (2019)

<https://doi.org/10.1063/1.5100215>



Articles You May Be Interested In

An adaptive mesh refinement-multiphase lattice Boltzmann flux solver for simulation of complex binary fluid flows

Physics of Fluids (December 2017)

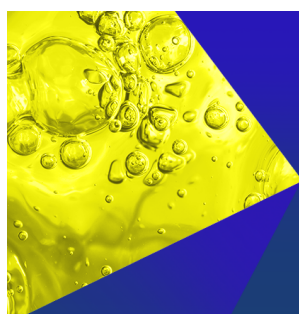
Computational modeling of three-dimensional thermocapillary flow of recalcitrant bubbles using a coupled lattice Boltzmann-finite difference method

Physics of Fluids (March 2021)

Development of closure relations for the motion of Taylor bubbles in vertical and inclined annular pipes using high-fidelity numerical modeling

Physics of Fluids (June 2020)

09 June 2025 05:03:45



Physics of Fluids
Special Topics
Open for Submissions

[Learn More](#)

Phase field lattice Boltzmann model for air-water two phase flows

Cite as: Phys. Fluids 31, 072103 (2019); doi: 10.1063/1.5100215

Submitted: 16 April 2019 • Accepted: 15 June 2019 •

Published Online: 11 July 2019



E. Dinesh Kumar,^{a)} S. A. Sannasiraj,^{b)} and V. Sundar^{c)}

AFFILIATIONS

Department of Ocean Engineering, Indian Institute of Technology Madras, Chennai 600036, India

^{a)}Electronic mail: edk261@gmail.com

^{b)}Electronic mail: sasraj@iitm.ac.in

^{c)}Electronic mail: vsundar@iitm.ac.in

ABSTRACT

Two phase flows occur in different forms with liquid and gas in general, among which, the interaction of the flow of air and water is a common scenario. However, modeling the two phase flow still remains a challenge due to the large density ratio between them and different space-time scales involved in the flow regimes. In the present work, the lattice Boltzmann (LB) model capable of handling large density ratio (1000) and high Reynolds number (10^4) simultaneously is proposed. The present model consists of two sets of LB equations, one for the flow field in terms of normalized pressure-velocity formulation and the other for the solution of the conservative Allen-Cahn equation to capture the interface. The numerical tests such as stationary drop, bubble coalescence, and capillary wave decay have been performed, and the results exhibit excellent mass conservation property. The capability of the present model to handle complex scenarios has been tested through test cases, for example, rise of an air bubble, splash of a water droplet on a wet bed, and Rayleigh-Taylor instability. In all test cases, the simulation results agree well with the available reference data. Finally, as an application of the present model, the breaking of a deep water wave with high Reynolds number (10^4) is simulated. The plunging breaker with wave overturning and the generation of secondary jet and splashes are well described by the present LB model. The evolution of wave energy dissipation during and after breaking is in agreement with the reference data.

Published under license by AIP Publishing. <https://doi.org/10.1063/1.5100215>

I. INTRODUCTION

Numerical modeling of two-phase flows constituting air and water poses challenges, in particular, due to the large density difference between them within the sharp interface and the different time/length scales involved in the different physical processes. While large length scales are involved such as the propagation of water waves, the simulation can be addressed without considering the role of air. The effect of air becomes significant when the wave breaks and bubbles/droplets of various sizes enhance the energy dissipation during the breaking process.¹ Earlier numerical models were based on methods such as finite-difference/element/volume schemes to obtain the solution for the Navier-Stokes (NS) equation. In the above methods, the representation of the interface is a challenging task when the flow involves topological changes like mixing, splashing, and entrapment of one fluid over another. Hence, interface schemes such as front tracking,² Volume of Fluid (VoF),³ and Level Set (LS)⁴ schemes have been developed in the past. Among these, VoF and

LS schemes have received considerable attention due to their Eulerian nature. Due to the lack of mass conservation in LS schemes and the challenge in the calculation of surface normal in VoF schemes, several remedies such as coupled LS-VOF were proposed. However, these improved versions result in the loss of simplicity and become computationally more expensive.

The mesoscale Lattice Boltzmann (LB) models have emerged as an alternate approach to continuum hypothesis based modeling. The inherent parallelism and simplicity are often cited as the major strengths for LB models, and these advantages cannot be taken for granted in understanding the basic physics under scenarios such as breaking of water waves. To reduce the computational burden as well as at times when the role of the other phase (air) is insignificant, free surface LB models can be used to study problems like metal foaming, bubble raising, and dam breaking.^{5,6} Since water has very low viscosity ($10^{-6} \text{ m}^2 \text{ s}^{-1}$) and if one considers the laboratory scale, the length scale for various physical processes may range from nanometers (bubbles/drops) to a few meters (waves). Thus, for the

real scenario, the stable and accurate computational fluid dynamics simulation resolving all scale regimes of a physical system is often quite tedious.

The development of two-phase LB models for large density ratio (ρ^*) flow problems has witnessed tremendous improvements for both the prediction of the flow field and the accurate representation of the interface. The successful major improvements were (i) pressure-velocity LB formulation instead of density-velocity formalism,⁷ (ii) Multiple Relaxation Time (MRT) collision operators,^{8,9} and (iii) directional derivatives for the force terms.¹⁰ Among these, the use of the directional derivative leads to violation of mass conservation especially in the pressure-velocity formulation.¹¹ Hence, the isotropic finite difference schemes for gradient and Laplacian operators were utilized and this in turn proved to be an added advantage in terms of both mass conservation and high computational performance than offered by directional derivatives.⁹ Due to the generic collision operator, the MRT model has been adopted to other LB models such as entropic LB¹² and cascaded LB¹³ for the simulation of fluid flows with high density and low viscosity ratio. The traditional LB flow solver describes the evolution of the number density distribution function, and its zeroth moment yields the density. In the physical space, density is a discontinuous field, whereas the pressure is a continuous one. Hence, for two-phase flows, the density-velocity formulation is prone to face instability at the interface.¹⁴ To overcome this discontinuity, most two phase models are based on pressure-velocity formulation, where the transformation function is used and correspondingly the pressure can be computed directly from the zeroth moment, instead of using the system's equation of state.^{8,10,15}

Most environmental flows involving air-water belong to high Reynolds number (Re) regime, and there exist quite a few LB models^{16,17} which can handle high Re and large ρ^* simultaneously. However, the maximum Reynolds number reported in these studies was around 6200,¹⁷ whereas the model proposed by Banari *et al.*¹⁸ can handle a high Re of 32 400. The approach of Banari *et al.*¹⁸ is similar to that of Inamuro *et al.*,¹⁹ wherein solving the pressure-Poisson equation through the lattice Boltzmann method (LBM) was utilized. However, the MRT-based phase field model⁸ does not involve pressure correction techniques, and the model has been validated for a density ratio of 100 (stationary bubble test) and a high Reynolds number of 30 000 (Rayleigh Taylor instability problem). Like most early works,^{7,8} Zu and He²⁰ proposed the two phase model for moderate density and viscosity ratios based on the pressure-velocity formulation. Based on the Zu and He²⁰ model, Fakhari *et al.*⁹ modified the transformation function with the normalized pressure term. This modified transformation leads to an increased stability for flows having moderate Reynolds numbers (3000) and fluids with large density ratio (1000).⁹

The multiphase flow simulation involves accurate representation of the interface between the fluids, and several schemes such as the two-component lattice gas model,²¹ pseudopotential model,²² free energy model,²³ front tracking method,²⁴ phase-field models^{8,9,20} and the level set method^{15,25} are utilized. Unlike VoF and LS schemes which solve the advection type equations, phase-field models solve the advection-diffusion equation such as Cahn-Hilliard (CH) equation. In order to improve the interface representation, hybrid LB schemes are proposed, wherein the flow field is solved

using the LBM but the phase-field equation is solved through finite difference schemes.^{26,27} Due to the locality in computation and simplicity in handling the sharp interfaces, LB-based phase field models are more attractive over the other models, particularly for fluids with large density ratio. In addition, the inclusion of surface tension force as an equivalent body force can be done easily in phase field models. Most LB phase field models adapted the CH equation for interface representation,^{8,18–20,28} but the CH equation poses certain difficulties in terms of computation (the existence of the fourth derivative of chemical potential) and the determination of model parameters (mobility). Hence, in order to improve the interface representation as well as to simplify the computation, the conservative Allen-Cahn (AC) equation was proposed.^{9,29,30}

Based on the above discussion, it is clear that the development of two phase LB models for high Re and large density ratio is a challenging task. While most of the earlier works are based on the pressure-velocity formulation, the present study employs the formulation of Fakhari *et al.*⁹ for the stability of the flow model with normalized pressure term. However, the interface scheme is adopted from the work of Ren *et al.*³⁰ which is an improved version of Geier *et al.*,²⁹ wherein to tackle complex topological changes at high Reynolds number, the MRT collision operator is introduced rather than the single relaxation time model of Refs. 9 and 29. Another major modification is the removal of higher order terms in the equilibrium distribution function and the inclusion of the time derivative of the phase function to recover the correct conservative AC equation.³⁰

The CH and AC equations in the conservative form imply the conservation of the phase function and consequently the conservation of mass.²⁹ Though the multiphase models indicated above^{8,9,20} can recover the exact momentum equation, the failure of mass conservation at the interface region was observed by Li *et al.*³¹ The interfacial force term which acts only at the interface was derived based on the CH equation.³¹ Ren *et al.*³⁰ derived a similar term suitable for the AC equation. The influence of the interfacial force term is more pronounced when the flows involve large density difference between the fluids and high Reynolds number simultaneously. This interfacial force term was not used in the work of Fakhari *et al.*⁹ as the test cases attempted belonged to moderate Reynolds number (up to 3000). Thus, the proposed two phase LB model consists of the flow model of Fakhari *et al.*⁹ with an added interfacial force term^{30,31} and the improved interface model.³⁰

This paper is organized as follows: Sec. II describes the theory of the LB model for the flow field and the interface. The numerical results are presented in Sec. III which includes the validation test cases, for example, stationary drop, bubble coalescence, and the decay of capillary wave. Later, the simulation results of the bubble rise phenomenon, splash of the droplet on a wet bed, Rayleigh-Taylor instability (RTI), and breaking waves are presented. A brief summary of results and conclusions are given in Sec. IV.

II. LATTICE BOLTZMANN MODEL FOR TWO PHASE FLOWS

A. LB model for interface

The present interface scheme is based on the conservative AC equation which describes the evolution of phase field ϕ ,³⁰

$$\frac{\partial \phi}{\partial t} + \nabla \cdot \phi \mathbf{u} = M_\phi [\nabla^2 \phi - \nabla \cdot (\theta \mathbf{n})], \quad (1)$$

where M_ϕ is the mobility coefficient, $\mathbf{n} = \nabla \phi / |\nabla \phi|$ is the normal vector, and $\theta = -4(\phi - \phi_H)(\phi - \phi_L)/(W(\phi_H - \phi_L))$, W represents the interface width, ϕ_L and ϕ_H are the phase indicators of low and high density fluids, respectively. In the equilibrium state, the profile for the phase function ϕ is given by

$$\phi(z) = \frac{\phi_H + \phi_L}{2} + \frac{\phi_H - \phi_L}{2} \tanh\left(\frac{2z}{W}\right). \quad (2)$$

The LB model for Eq. (1) can be written as³⁰

$$h_i(\mathbf{x} + \mathbf{e}_i \Delta t, t + \Delta t) - h_i(\mathbf{x}, t) = \Omega_{ij}^h (h_j^{eq} - h_j)|_{(\mathbf{x}, t)} + \Delta t F_i^\phi(\mathbf{x}, t), \quad (3)$$

where Ω_{ij}^h represents the element of the collision matrix and can be obtained from $\Omega = \mathbf{M}^{-1} \mathbf{S} \mathbf{M}$, where \mathbf{M} is the matrix that transforms distribution functions into moment space. The relaxation matrix, \mathbf{S} , is diagonal and is written as $\mathbf{S} = [s_0^h, s_1^h, \dots, s_8^h]$, with $s_3^h = s_5^h = 1/\tau^h$. The mobility, M_ϕ , can be linked to the relaxation parameter $M_\phi = (\tau^h - 0.5)c_s^2$ and is often cited as an advantage when compared to the CH equation, where the mobility depends on an additional constant η , $M_\phi = \eta c_s^2 (\tau^h - 0.5)$.^{8,31} The equilibrium distribution function $h_i^{eq} = \omega_i \phi (1 + c_s^{-2} \mathbf{e}_i \cdot \mathbf{u})$, where \mathbf{e}_i and ω_i are lattice velocity and weight coefficients corresponding to i th direction, respectively, and c_s is the sound speed. The source term $F_i^\phi = \omega_i \theta \mathbf{e}_i \cdot \mathbf{n} + \omega_i c_s^{-2} \mathbf{e}_i \cdot \partial_t (\phi \mathbf{u})$, where the evaluation of the temporal derivative has been done using the first order Euler's scheme.

The present interface model³⁰ has few distinct capabilities compared to other models,^{9,29} viz., (i) the use of the MRT collision operator, (ii) inclusion of the time derivative of phase-field flux, and (iii) absence of nonlinear terms in the equilibrium distribution function. It has been stated that the role played by the time derivative term of phase-field flux is insignificant,⁹ but it has been included in the present formalism so as to fulfill the exact recovery of the conservative AC equation through the Chapman-Enskog analysis.³⁰

The order parameter ϕ can be computed as $\phi = \sum_i h_i$, and the values of density ρ and viscosity ν are obtained through the linear interpolation,

$$\begin{aligned} \rho(\phi) &= \rho_L + \frac{\phi - \phi_L}{\phi_H - \phi_L} (\rho_H - \rho_L), \\ \nu(\phi) &= \nu_L + \frac{\phi - \phi_L}{\phi_H - \phi_L} (\nu_H - \nu_L). \end{aligned} \quad (4)$$

B. LB model for flow

The continuity and the incompressible Navier-Stokes equation govern the evolution of the flow field and can be written as

$$\begin{aligned} \nabla \cdot \mathbf{u} &= 0, \\ \rho \left(\frac{\partial \mathbf{u}}{\partial t} + \mathbf{u} \cdot \nabla \mathbf{u} \right) &= -\nabla p + \nabla \cdot [\nu \rho (\nabla \mathbf{u} + \nabla \mathbf{u}^T)] + \mathbf{F}, \end{aligned} \quad (5)$$

where ρ , ν , p , and \mathbf{F} denotes the density, kinematic viscosity, pressure, and the external force, respectively. To solve Eq. (5), we start

with the discrete Boltzmann equation Eq. (6), which describes the evolution of the particle density distribution function (PDF) f_i ,^{9,20}

$$\left(\frac{\partial}{\partial t} + \mathbf{e}_i \cdot \nabla \right) f_i = \Omega_{ij}^f (f_j^{eq} - f_j) + F_i, \quad (6)$$

where $f_i^{eq} = \omega_i \rho + \rho s_i(\mathbf{u})$ is the equilibrium distribution function with

$$s_i(\mathbf{u}) = \omega_i \left[\frac{(\mathbf{e}_i \cdot \mathbf{u})}{c_s^2} + \frac{(\mathbf{e}_i \cdot \mathbf{u})^2}{2c_s^4} - \frac{(\mathbf{u} \cdot \mathbf{u})}{2c_s^2} \right] \quad (7)$$

and $\Gamma_i(\mathbf{u}) = f_i^{eq}/\rho$. At first, the distribution function f_i is transformed into g_i so as to obtain the improved pressure-velocity formulation²⁰

$$g_i = \begin{cases} \frac{f_i}{\rho} + (p^* - 1)\Gamma_i(0) - p^*, & i = 0, \\ \frac{f_i}{\rho} + (p^* - 1)\Gamma_i(0), & i \neq 0, \end{cases} \quad (8)$$

where $p^* = p/(\rho c_s^2)$ is the normalized pressure. The corresponding evolution equation for g_i can be written as

$$\frac{Dg_i}{Dt} = \left(\frac{\partial}{\partial t} + \mathbf{e}_i \cdot \nabla \right) g_i = \Omega_{ij}^f (g_j^{eq} - g_j) + F_i, \quad (9)$$

where the equilibrium function g_i^{eq} and force F_i are given by

$$\begin{aligned} g_i^{eq} &= \begin{cases} p^* (\omega_i - 1) + s_i(\mathbf{u}), & i = 0, \\ p^* \omega_i + s_i(\mathbf{u}), & i \neq 0, \end{cases} \\ F_i &= \Delta t \omega_i \frac{\mathbf{e}_i \cdot \mathbf{F}}{\rho c_s^2}. \end{aligned} \quad (10)$$

Integration of Eq. (9) using the trapezoidal rule yields

$$\begin{aligned} g_i(\mathbf{x} + \mathbf{e}_i \Delta t, t + \Delta t) - g_i(\mathbf{x}, t) &= \frac{\Delta t}{2} [\Omega_{ij}^f (g_j^{eq} - g_j) + F_i] \Big|_{(\mathbf{x} + \mathbf{e}_i \Delta t, t + \Delta t)} \\ &\quad + \frac{\Delta t}{2} [\Omega_{ij}^f (g_j^{eq} - g_j) + F_i] \Big|_{(\mathbf{x}, t)}. \end{aligned} \quad (11)$$

In order to remove the implicitness in Eq. (11), the following transformation is used:

$$\tilde{g}_i = g_i - \frac{\Delta t}{2} [-\Omega_{ij}^f (g_j - g_j^{eq}) + F_i]. \quad (12)$$

The corresponding modified equilibrium distribution function would be

$$\tilde{g}_i^{eq} = g_i^{eq} - \frac{\Delta t}{2} F_i. \quad (13)$$

Thus, the final LB model for flow becomes

$$\tilde{g}_i(\mathbf{x} + \mathbf{e}_i \Delta t, t + \Delta t) - \tilde{g}_i(\mathbf{x}, t) = -\Omega_{ij}^g (\tilde{g}_j - \tilde{g}_j^{eq}) + \Delta t F_i. \quad (14)$$

The total force, \mathbf{F} , is composed of surface forces (pressure gradient, surface tension, and shear) and body force (gravity). Thus,

$$\mathbf{F} = \mathbf{F}_p + \mathbf{F}_b + \mathbf{F}_s + \mathbf{F}_\mu + \mathbf{F}_a, \quad (15)$$

where $\mathbf{F}_p = -p^* c_s^2 \nabla \rho$, \mathbf{F}_b is the body force, $\mathbf{F}_s = \mu \nabla \phi$ is the surface tension with the chemical potential

$$\mu = 4\beta(\phi - \phi_H)(\phi - \phi_L)\left(\phi - \frac{\phi_H + \phi_L}{2}\right) - k\nabla^2 \phi,$$

and the coefficients

$$\beta = \frac{12\sigma}{W(\phi_H - \phi_L)^4} \text{ and } \kappa = \frac{3W\sigma}{2(\phi_H - \phi_L)^2}.$$

The viscous force plays a major role in maintaining the stability when the flow regime has high Reynolds number. The computation of viscous force involves the computation of stress tensor and is performed locally using the equilibrium part of the distribution function. A similar calculation has been performed in the Large Eddy Simulation (LES) model,³² but the computed stress tensor is used to correct the relaxation time, whereas, in the present two phase model, it is treated as a force term.⁹ Apart from the LES and the present formulation, another approach called fractional step algorithm has been proposed, wherein the corrective viscous force term is added via the solution obtained from the first order advection equation at each time step.^{33,34} Thus, the viscous force $\mathbf{F}_\mu = -\nu[\nabla\mathbf{u} + \nabla\mathbf{u}^T] \cdot \nabla\rho$ can be computed locally as⁹

$$\mathbf{F}_{\mu,i} = \frac{-\nu}{c_s^2 \Delta t} \left[\sum_{\beta} e_{\beta i} e_{\beta j} \times \sum_{\alpha} \Omega_{\beta\alpha}^g (g_{\alpha} - g_{\alpha}^{eq}) \right] \frac{\partial \rho}{\partial x_j}. \quad (16)$$

At the interface, phase field LB models fail to satisfy the continuity equation and, hence, an additional interfacial force $\mathbf{F}_a = -q\mathbf{u}$ is needed to satisfy the incompressibility criterion throughout the domain.³¹ The evaluation of term q in \mathbf{F}_a can be done using the following relation:³⁰

$$q = \frac{\partial p}{\partial t} + \nabla \cdot \rho \mathbf{u} = \frac{\partial p}{\partial \phi} \left(\frac{\partial \phi}{\partial t} + \nabla \cdot \phi \mathbf{u} \right) = \frac{\partial p}{\partial \phi} M_{\phi} [\nabla^2 \phi - \nabla \cdot (\theta \mathbf{n})]. \quad (17)$$

Finally, the macroscopic variables, velocity and pressure, can be computed as

$$\mathbf{u} = \frac{\sum_i \mathbf{e}_i \tilde{g}_i + 0.5 \Delta t p^{-1} (\mathbf{F}_p + \mathbf{F}_s + \mathbf{F}_b + \mathbf{F}_{\mu})}{1 - 0.5 \rho^{-1} q}, \quad (18)$$

$$p = \rho c_s^2 p^* = \rho c_s^2 \sum_i \tilde{g}_i. \quad (19)$$

III. NUMERICAL RESULTS

In all test cases, unless otherwise stated, the density ratio is set to 1000 and the kinematic viscosity ratio to 10 to match the air-water system. The phase indicators, ϕ_H and ϕ_L , take the value of 1 and 0, respectively. The computer code has been built based on the open-source LB framework, TCLB.^{35,36}

A. Stationary drop

The stationary drop test is performed to validate the multiphase model for mass conservation and existence of spurious velocity in the flow field. A circular water drop of radius R is placed at the center of a periodic domain of length L filled with air. According to the Laplace law, the pressure difference Δp between inside and outside of the drop is related to the surface tension σ and radius R by $\Delta p = \frac{\sigma}{R}$, provided no external forces such as gravity act on it. The computational domain of unit length in both the axis is discretized into 128×128 lattice nodes. The relaxation parameter τ_g for the flow field is chosen by fixing lattice viscosity $\nu_{lb} = 0.005$. The other parameters

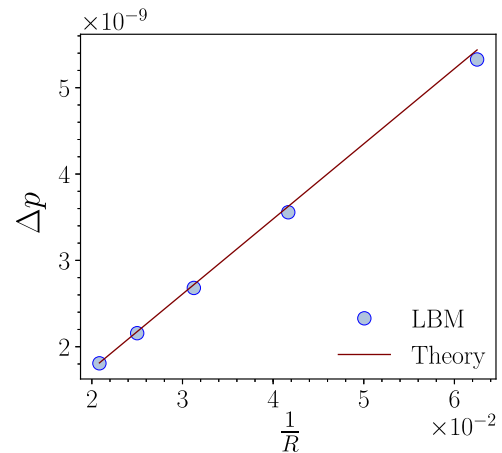


FIG. 1. Comparison of pressure difference between the inside and the outside of the drop with the Laplace law.

are the following: interface width $W = 5$, surface tension $\sigma = 8.7 \times 10^{-5}$, and mobility $M_{\phi} = 1$. At the initial time, both the velocity and pressure field are set to zero. Five different radii of the drop $R = 16, 24, 32, 40, 48$ (in lattice units, lu) are considered.

After the drop has reached the equilibrium state, Δp has been computed and the variation plotted against R^{-1} (Fig. 1). Though the results show the satisfactory agreement with the theory, the model's performance can be assessed by estimating the following parameters: (i) percentage of relative difference $[\|\cdot\| = (\text{exact} - \text{lbm})/\text{exact} \times 100]$ for Δp and the total mass of the drop M and (ii) maximum velocity $U_{max} = (\sqrt{u^2 + v^2})_{max}$.

The relative differences of both Δp and M are within the tolerable limit (Table I). In the case of Δp , the exact solution is available to compute relative difference, but for $\|M\|$, the initial mass is taken as the reference value. The exact mass conservation is observed in all cases except for $R = 16$. This shows that the bubble radius has to be relatively large when compared with the interface width. The maximum magnitude of spurious velocity U_{max} found near the interface is of $O(10^{-10})$. Thus, the present model satisfies the mass conservation and a minimal spurious velocity simultaneously.

B. Bubble coalescence

The process of bubble merging involves complex topological changes, which includes the formation of the microscale bridge

TABLE I. Relative difference (in %) of Δp and mass M along with the maximum spurious velocity for the stationary drop test.

R	$\ \Delta p\ $	$\ M\ $	U_{max}
16	2.00	1.6×10^{-6}	4.18×10^{-11}
24	1.8	0	1.04×10^{-10}
32	1.40	0	1.96×10^{-10}
40	0.8	0	3.02×10^{-10}
48	0.3	0	5.24×10^{-10}

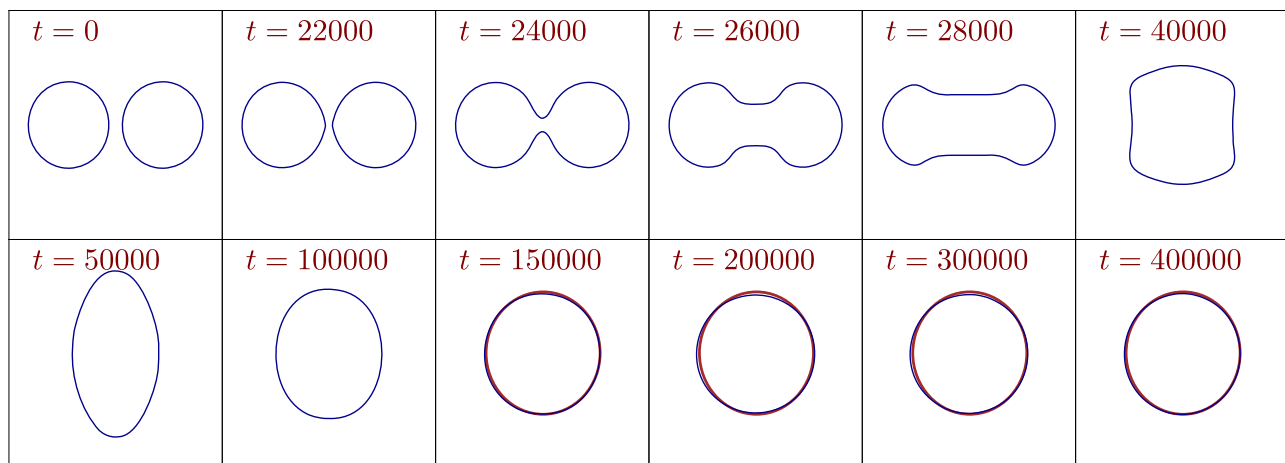


FIG. 2. Evolution of bubble coalescence (theoretical limit is plotted in red after $t \geq 150\,000$).

between the bubbles at their initial stage of contact. Two stationary bubbles of equal radius R have been separated by a distance, d , that is not greater than twice of the interface thickness W . The condition $d < 2W$ is necessary for the bubbles to merge³⁷ because the surface tension, σ , is the key parameter which depends on W through the coefficients β and κ in chemical potential μ .

The computational setup is the same as in the stationary drop test case except that the present one is a bubble, whereas the previous case involves drop. At the initial time, bubbles are located at co-ordinates (32,64) and (92,64) with radius of $R = 24$ (in lu). Figure 2 shows the evolution of bubble coalescence at different instants of time (in lu). Three key features are observed, viz., formation of bridge between the bubbles, dumb-bell shape, and the elliptical shape prior to the equilibrium circular shape. These shape evolutions are consistent with the earlier studies (refer to Fig. 6 in Ref. 37 and Fig. 8 in Ref. 25), where the values for density and viscosity ratios are taken similar to the present work. After the time steps $t \geq 15 \times 10^4$, the newly formed bubble has a circular shape which is compared with the theoretical estimate, i.e., the radius of new bubble will be $R_{new} = R\sqrt{2}$ (in 2D). The final circular bubble has a radius of $R_{lbm} = 33.47$ while the theoretical radius is $R_{theory} = 33.94$. It yields the relative difference error of 1.38%. This proves that the present algorithm obeys the mass conservation.

C. Capillary wave

The propagation of capillary wave is an unsteady process and enables us to verify the capability of the model to handle all the crucial physical parameters such as density ratio, viscosity ratio, and surface tension. The simulation is carried out by varying viscosity and the wavelength so as to verify the model's prediction of wave elevation and angular frequency with that of the linear theory. Let the density of the fluid on the top be ρ_L and that of at the bottom be ρ_H with the interface located at $y = L + \eta_0 \cos(kx)$, where η_0 is the initial amplitude (Fig. 3). The initial small wavy profile decays to the flat surface, solely due to the viscosity and the surface tension, as there are no external forces such as gravity acts on the flow field. The decay of wave amplitude $\eta(t)$ can be derived analytically³⁸ and

is given by

$$\frac{\eta(t)}{\eta_0} = \frac{4(1-4\gamma)v^2k^4}{8(1-4\gamma)v^2k^4 + \omega_0} \operatorname{erfc}(\sqrt{vk^2t}) + \sum_{i=1}^4 \frac{z_i}{Z_i} \frac{\omega_0^2}{z_i^2 - vk^2} e^{(z_i^2 - vk^2)t} \operatorname{erfc}(z_i\sqrt{t}), \quad (20)$$

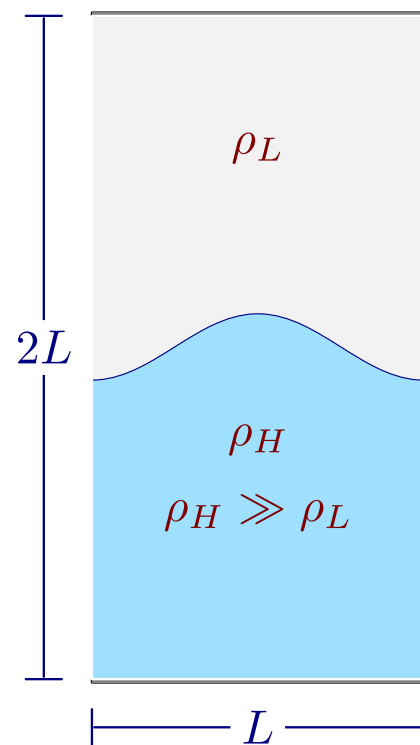


FIG. 3. Schematic diagram of capillary wave propagation.

TABLE II. Relative difference (in %) of ω .

L	32	64	128
ν	0.005	0.005	0.005
$\ \omega\ $	5.03	0.99	0.5

where $\omega_0 = \sqrt{\frac{\sigma k^3}{\rho_H + \rho_L}}$ is the angular frequency, $\gamma = \frac{\rho_H \rho_L}{(\rho_H + \rho_L)^2}$ and $Z_i = \prod_{1 \leq j \leq 4, j \neq i} (z_j - z_i)$. The evaluation of complementary error function $\text{erfc}(z_i)$ can be done by solving the following algebraic equation:

$$z^4 - 4\gamma\sqrt{\nu k^2} z^3 + 2(1 - 6\gamma)\nu k^2 z^2 + 4(1 - 3\gamma)(\nu k^2)^{\frac{3}{2}} z + (1 - 4\gamma)\nu k^2 + \omega_0^2 = 0. \quad (21)$$

The computational domain is discretized into 128×256 lattice nodes with periodic boundary condition applied in the direction of wave propagation and slip condition at the top and bottom boundaries. The other simulation parameters (in lu) are set to $\eta_0 = 0.02$,

$\sigma = 10^{-4}$, $W = 5$, and $M_\phi = 0.02$. Since the interface may not coincide exactly at the grid point, the values of $\eta(t)$ can be computed using the values of ϕ through interpolation,³⁷

$$\eta(t) = iy - \frac{\phi(iy)}{\phi(iy) - \phi(iy - 1)}, \quad \phi(iy)\phi(iy - 1) < 0. \quad (22)$$

The length (η) and time scales (t) are normalized by the initial amplitude a_0 and the angular frequency ω_0 , respectively ($\eta^* = \eta/\eta_0$ and $t^* = t\omega_0$).

The angular frequency is the most important parameter for any wavy system. In the present case, angular frequency depends on surface tension, wave number, and density values. Except the wave number, other two parameters have been fixed and hence three different wavelengths (in lu) $L = 32, 64, 128$ have been considered. Note that the magnitude of the wavelength equals the grid size. Equation (20) has been derived based on the assumption that both the fluids possess the same viscosity,³⁸ and we choose $\nu = 0.005$. Since the relaxation parameter, τ , depends on the viscosity of the fluid, three different values for viscosity, $\nu = 0.0005, 0.01, 0.02$ are employed for the case $L = 128$.

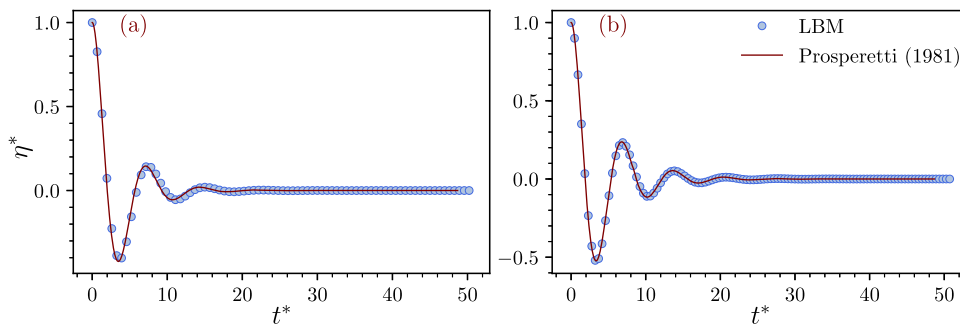
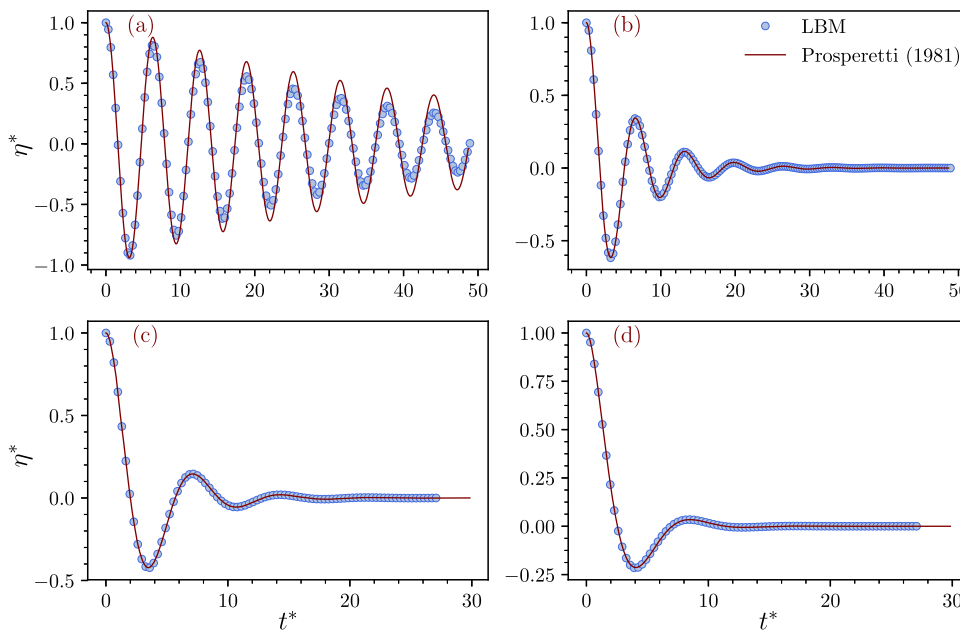

 FIG. 4. Evolution of capillary wave amplitude for $\nu = 0.005$ with (a) $L = 32$ and (b) $L = 64$.

 FIG. 5. Evolution of capillary wave amplitude for $L = 128$ with four different viscous values: (a) $\nu = 0.0005$, (b) $\nu = 0.005$, (c) $\nu = 0.01$, and (d) $\nu = 0.02$.

TABLE III. Comparison of predicted Re with the experiment⁴⁰ and simulation results of Hua *et al.*⁴¹

Case	Bo	Mo	Re			$\frac{ Re_{Expt}-Re_{LBM} }{Re_{Expt}} \times 100$	$\frac{ Re_{Expt}-Re_{FVM} }{Re_{Expt}} \times 100$
			LBM (present)	Experiment ⁴⁰	NS-FVM ⁴¹		
A1	17.7	711	0.26	0.232	0.182	12.07	21.55
A2	32.2	8.2×10^{-4}	57.55	55.3	54.79	4.07	0.92
A3	243	266	10.68	7.77	7.605	37.45	2.12
A4	115	4.63×10^{-3}	99.6	94.0	89.64	5.96	4.64
A5	339	43.1	19.76	18.3	17.75	7.97	3.0

Initially, the percentage of relative difference for the simulated angular frequency with that of theory has been computed for all test cases. Except the case of $L = 32$ with $\nu = 0.005$, all the other cases show an agreement with an error of $\leq 1.5\%$ (Table II). The evolution of normalized wave amplitude η^* enables us to identify the capability of the model in handling the forces for the simulation that require larger time steps. The present results show that the captured wave peaks (crests and trough) are in agreement (Figs. 4 and 5) for all cases, except the lower viscous case ($L = 32$ with $\nu = 0.005$), where the decay rate is much faster than that of theory [Fig. 5(a)]. Thus, the accuracy of angular frequency depends on the grid size

and the wave elevation depends on the chosen viscosity, while the other simulation parameters are fixed.

D. Rise of a single bubble in quiescent fluid

The rise of a spherical bubble in a quiescent liquid is a preliminary test to verify two phase models. The balance of buoyancy, viscous, and surface tension forces are required for the correct prediction of the terminal velocity U_t and the shape of the bubble. The most common approach is to verify the prediction with experimental observations. The classification of flow regimes is based on

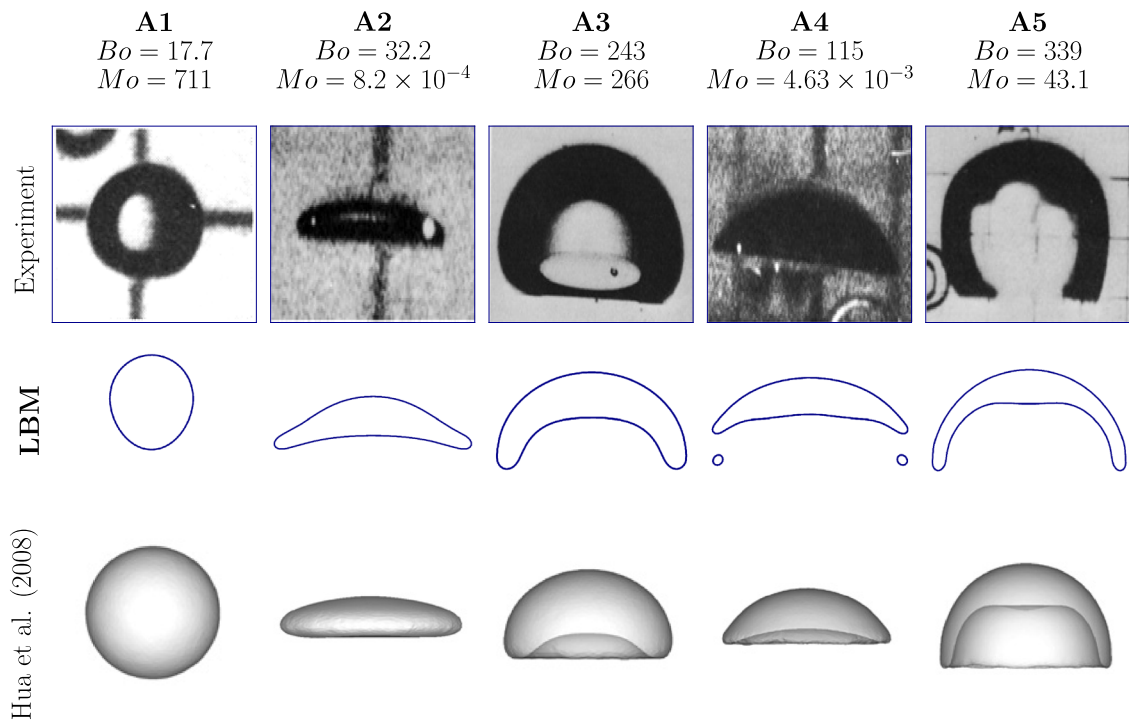


FIG. 6. Comparison of bubble's terminal shape with the experiment⁴⁰ [reproduced with permission from D. Bhaga and M. E. Weber, "Bubbles in viscous liquids: Shapes, wakes and velocities," J. Fluid Mech. **105**, 61 (1981); copyright 2006 Cambridge University Press] and simulation results of Hua *et al.*⁴¹ [reproduced with permission from J. Hua, J. F. Stene, and P. Lin, "Numerical simulation of 3d bubbles rising in viscous liquids using a front tracking method," J. Comput. Phys. **227**, 3358–3382 (2008); copyright 2008 Elsevier].

four dimensionless numbers, viz., density and viscosity ratios, Bond number ($Bo = \rho_H g D^2 / \sigma$), and Morton number ($Mo = g \mu_H^4 / \rho_H \sigma^3$). In the definitions, Mo completely depends on the fluid properties and is used to identify the relative importance of viscous to surface tension forces. On the other hand, Bo depends on the bubble diameter and represents the effects of buoyancy to surface tension. Since the density and viscosity ratios are fixed, five different test cases with different Bond and Morton numbers are chosen for simulations

(Table III). The values are chosen to represent the different bubble regimes classified by Clift *et al.*³⁹ The computational domain is discretized into 256×512 nodes with periodic condition applied on the lateral direction and wall boundary on the vertical directions. Initially, both the fluids are kept stationary. The circular bubble of diameter $D = 48$ (lu) is placed at the co-ordinate (128, 72).

At the initial time, the bubble is circular (spherical in 3D) in shape and due to unsteady nature of the flow, the bubble shape

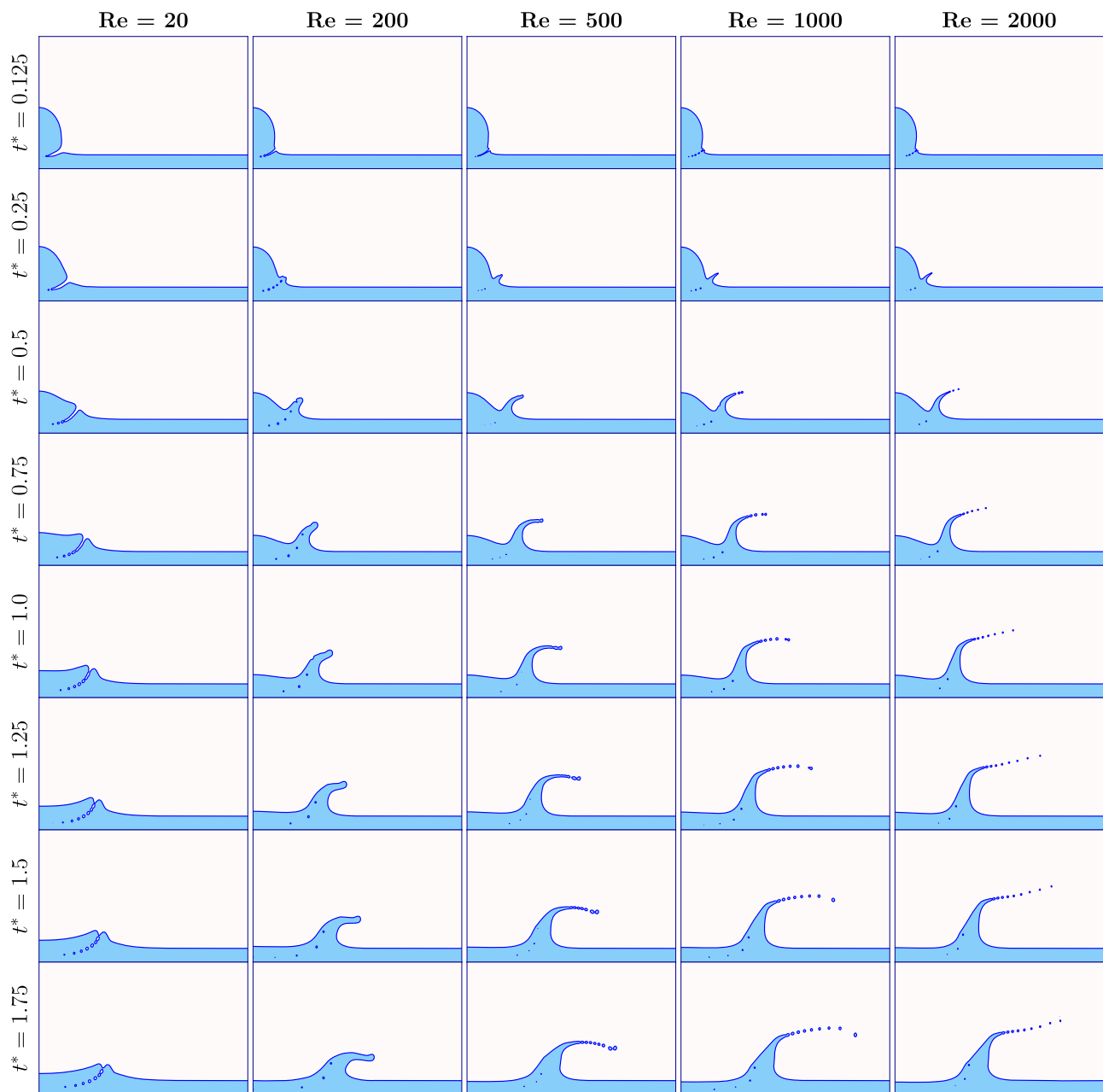


FIG. 7. Evolution of the falling droplet on a thin wet bed for five different Reynolds numbers (only the symmetric part has been presented).

may change from circular to different shapes, such as ellipsoidal, skirted, etc., or it may remain circular if the surface tension is strong. The observed terminal bubble shapes from experiments for test cases A1–A5 are spherical, oblate elliptical disk, oblate elliptical cap, spherical cap, and skirted, respectively.⁴⁰ Figure 6 shows a comparison of terminal bubble shapes with the experimental observations⁴⁰ and the three dimensional finite volume NS solutions.⁴¹ Expected terminal shape has been observed in all test cases. Due to high Re, case A4 results in the emergence of smaller bubbles out of the larger one, yet the terminal shape is close to the experiment. As the bubble reached the equilibrium stage, the terminal velocity U_t has been computed for each test case, and then used to compute the Reynolds number ($Re = U_t D / \nu_H$). Though the satisfactory comparison of Re has been observed from Table III, LB predicts a higher value than experiments in all test cases. The overestimation of U_t can be attributed to the density⁴² and viscosity⁴³ ratios adopted in the simulation. The reasonable terminal shape has been obtained for case A3, which has both moderate Bo and Mo, but at the cost of higher terminal velocity. It is to be noted that both Amaya-Bower and Lee⁴³ and Huang *et al.*⁴² have obtained the reasonable terminal shape that is comparable with the experiment. The density ratio of 1000 has been used in Amaya-Bower and Lee,⁴³ but the model of Huang *et al.*⁴² reached only up to the ratio of 15.5. In the case of terminal velocity, Huang *et al.*⁴² reported that the increase in density ratio increases the terminal velocity. Amaya-Bower and Lee⁴³ observed the instability due to decrease in viscosity ratio with low Morton number. The present simulation with low Mo numbers (cases A2 and A4) is found to be stable as well as in close agreement with the experiments (Table III).

E. Droplet splash on a thin wet bed

The impact of liquid droplets on a solid/liquid surface is a fascinating phenomenon especially if the impact exhibits splashes. The outcome of droplet impact on a wet bed made up of the same liquid results in either deposition or splashing. The dimensionless numbers used to characterize these flows are Reynolds number ($Re = \rho_H U D / \mu_H$) and Weber number ($We = \rho_H U^2 D / \sigma$), where ρ_H is the liquid density, U is the impact velocity, and D is the droplet diameter. Flows with higher We and Re numbers usually generate splashes/jet upon impact. The simulation has been carried out with a Weber number, $We = 8000$, and with five different Reynolds number, $Re = 20, 200, 500, 1000$, and 2000 . Physically, for a water drop of radius of order 1 mm, the variations in Re represent the variations in the impact velocity, which ranges between 0.01 and 1 ms^{-1} . The computational setup consists of a liquid droplet of radius R with density ρ_H and is placed above a wet bed of height H . The domain is discretized into 1024×256 lattice nodes with $R = 52$ and $H = 26$. Periodicity is applied on left and right boundaries, whereas no-slip is applied on top and bottom boundaries.

Figure 7 shows an evolution of droplet impact at various instants of dimensionless time ($t^* = Ut/D$). At the initial time, the drop has been kept at the surface of the bed with an initial impact velocity. For low Reynolds number ($Re = 20$), the droplet gradually spreads over the bed with an outward propagation of surface wave resulting in the deposition. On the other hand, for $Re \geq 200$, the liquid jet emerges upon impact. The jet emerged for the case of $Re = 200$ is so strong as it is not affected by viscous and surface

tension forces. However, for higher Re, the jet suffers from Rayleigh-Plateau instability (RPI) resulting in the generation of secondary droplets. The emergence of multiple secondary droplets has not been observed in the earlier phase field LB models^{26,28,44} which adopted the same parameters as in the present study. In addition, the influence of Reynolds number is observed from the direction of propagation of droplets. For $Re = 500$ and 1000 , the droplets are falling toward the bed after their generation but for $Re = 2000$, the droplets tend to move upward. Earlier, Josserand and Zaleski⁴⁵ have shown that at shorter duration, the viscous effects are negligible and the spread factor $r^* = r/D$ obeys the power law, i.e., $r^* = C\sqrt{t^*}$, where C is the constant obtained from the best fit. The log-log plot of spread factor r^* is shown in Fig. 8, and the fit coefficient was found to be $C = 1.065$, whereas $C = 1.1$ was proposed by Josserand and Zaleski.⁴⁵ The relative difference of around 3%. The key difference is the density ratio, which is set to 1000 in the present study, whereas it was set to 500 in Ref. 45. Thus, the present model is found to obey the power law proposed by Josserand and Zaleski.⁴⁵

F. Rayleigh-Taylor instability

The Rayleigh-Taylor instability (RTI) occurs due to the acceleration of high density fluid onto a low density fluid. The interface between the fluids is perturbed to create an instability which leads to the complex topological change of the interface geometry. The computational domain size is taken as $[0, L] \times [0, 4L]$ with $L = 256$, and the interface is located at $y_0(x) = 2L + 0.1L \cos(2\pi x/L)$. The periodic boundary condition is applied at the left and right boundaries, whereas no-slip condition is applied at the top and bottom boundaries. The characterization of RTI is through the following dimensionless numbers: Atwood number $At = (\rho_H - \rho_L)/(\rho_H + \rho_L)$, Reynolds number $Re = \rho_H U_0 L / \mu_H$ with $U_0 = \sqrt{gL}$, Capillary number $Ca = \mu_H U_0 / \sigma$, and Peclet number $Pe = U_0 L / M$. The reference

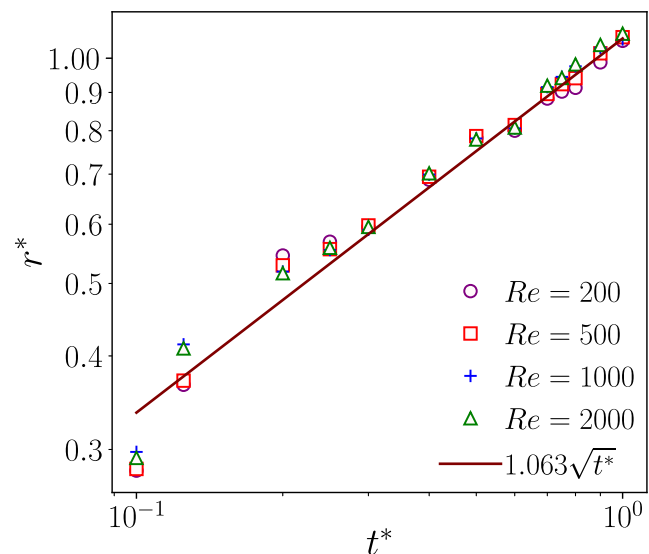
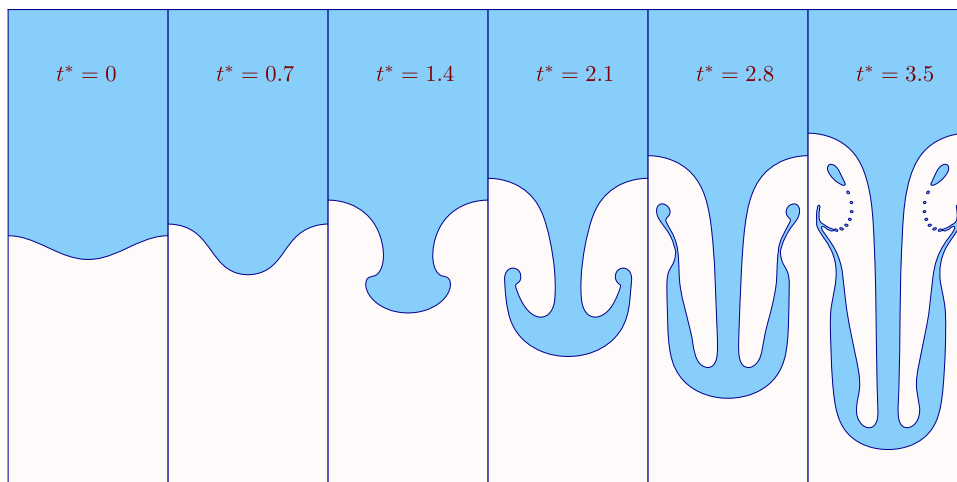
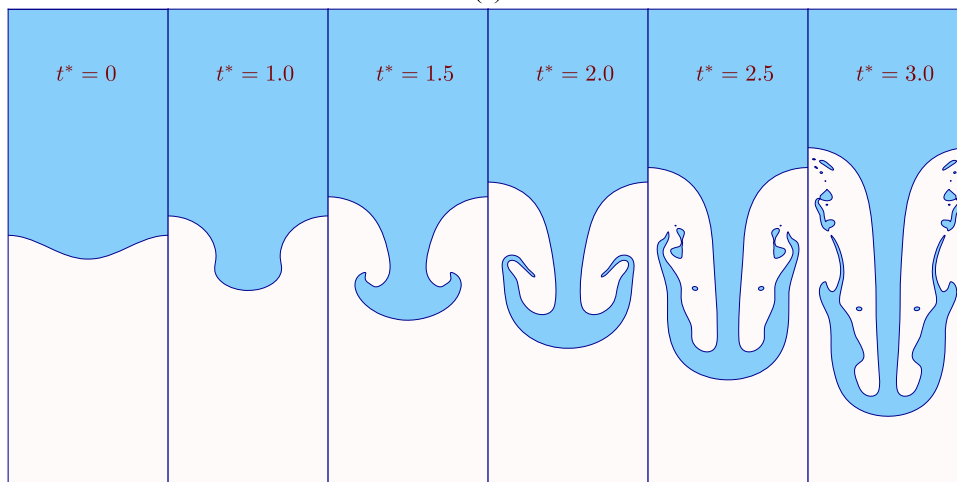


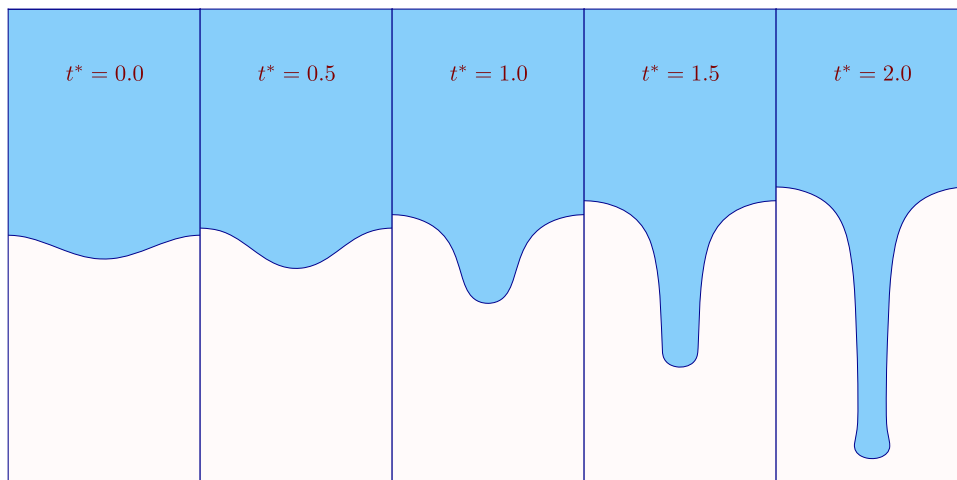
FIG. 8. Evolution of spread factor (log-log scale).



(a)



(b)



(c)

FIG. 9. Time evolution of density contours of RTI. (a) $At = 0.5$, $Re = 256$, $\mu^* = 3$, $Ca = 0.26$, and $Pe = 500$; (b) $At = 0.5$, $Re = 3000$, $\mu^* = 1$, $Ca = 0.26$, and $Pe = 1000$; and (c) $At = 0.998$, $Re = 3000$, $\mu^* = 100$, $Ca = 0.44$, and $Pe = 1000$.

length and time scale are taken as L and $\sqrt{L/|gAt|}$, respectively [$y^* = y/L$ and $t^* = t\sqrt{|gAt|/L}$].

Three different test cases (refer to the caption of Fig. 9 for parameters) are performed, and the results are compared with the previous studies.^{7,9,30} From Figs. 9(a) and 9(b), the following flow features are identified: (i) downward growth of initial perturbation, (ii) rise of lighter fluid and the fall of heavier fluid, (iii) roll-up of primary spike and the subsequent generation of secondary spike in the upward direction, and (iv) breakup of secondary spike into multiple droplets. Though the above features are in good agreement with the earlier LB simulations,^{7,9,30} they are qualitative in nature. The quantitative comparison has been made by describing the time evolution of positions of spike (position of the interface at $x = L/2$) and bubble-front (at $x = 0$) (Fig. 10). The comparison is in good agreement with the reference LB simulation.^{7,9,30} The influence of Reynolds number in RTI flows can be observed through the emergence of multiple droplets at much earlier times for flow with high Re [Fig. 9(b)]. Few studies have been attempted to simulate RTI with large density ratio and high Reynolds number simultaneously.⁹ Based on the test case from Ref. 9, the simulation is performed with fluids having a density ratio of 1000 and high Reynolds number ($Re = 3000$). The comparison of Fig. 9(c) with that of Fig. 7 of Fakhari *et al.*⁹ shows a satisfactory agreement except for a minor difference noticed in the spike shape at $t^* = 2$.

C. Breaking wave

Surface waves' breaking in the ocean's deep water regime is extremely an complex and turbulent phenomenon. Breaking of deep water waves similar to the test case in Refs. 46 and 47 is simulated. The computational domain is a square of size equal to the wavelength L and is discretized into 512×512 nodes with periodic boundary condition on the horizontal direction. The slip condition is imposed on the top and bottom boundaries. At $t = 0$, the interface η is given by Stokes' third order wave profile

$$\eta(x, 0) = \frac{L}{2} + a \cos(kx) + \frac{1}{2}a^2k \cos(2kx) + \frac{3}{8}a^3k^2 \cos(3kx), \quad (23)$$

where L is the wavelength, $k = 2\pi/L$ is the wave number and a is an initial amplitude. The initial velocity field for water is taken as $u(x, 0) = \Omega a e^{ky} \cos(kx)$ and $v(x, 0) = \Omega a e^{ky} \sin(kx)$, where $\Omega = \sqrt{gk(1 + a^2k^2)}$. The initial steepness of $ak = 0.55$ is chosen. The simulation is performed for high Reynolds and Bond number values: $Re = 10^4$ and $Bo = 10^4$. The physical length scales corresponding to Re and Bo are around 2.5 cm and 27 cm, respectively.⁴⁶ These length scales correspond to the short gravity waves. The higher Re may require finer mesh size to resolve for boundary layers, but the present mesh size is sufficient to describe the global quantities such as total energy.⁴⁸

The plunging breaker is observed in the present simulation which is consistent with the earlier simulation performed using NS-volume of fluid^{46,49} and NS-level set⁴⁷ methods. The process of wave breaking includes the following: wave overturning, development of jet and its subsequent impingement on the water surface, generation of secondary jet and the splashes, and, finally, decay of wave toward the flat surface. Figure 11 shows that the present model captured the above processes involved in the breaking mechanism. Following Refs. 46 and 47, the time scale is normalized by the fundamental wave period ($t^* = t/T_f$, $T_f = \sqrt{gk}$). For large amplitude waves, the surface tension forces can play a role at tip of the plunging jet by altering the sharp front to round shaped front.⁵⁰ Since Bo is large and the initial steepness is high, the magnitude of surface tension plays an insignificant role to alter the type of wave breaking, i.e., plunging.^{51,52} Hence, the representation of F_s plays a significant role in the shape of the plunging jet. The shape of the plunging jet depends on the velocity vectors at the interface nodes, which in turn depends on the form of F_s . Due to the difference in surface tension representation in LB models, the significant changes in the velocity and pressure at the interface have been observed by Chao.⁵³ Thus, the difference in surface tension representation caused the variation in the jet shape between the present and earlier studies.^{46,47,49}

The initial steepness chosen in the present study is high enough to initiate the breaking within one wave period T_C of time (T_C is computed from the phase speed, $C = \sqrt{(g/k)(1 + (ak)^2)}$). Figure 12 shows the streamlines and contour of the velocity field at the time

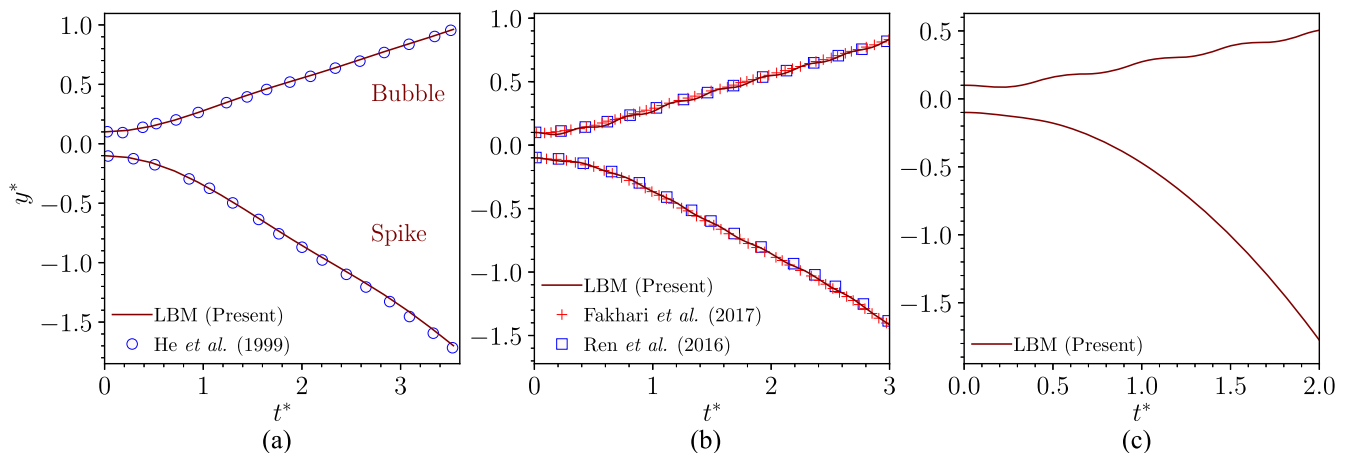


FIG. 10. Time evolution of bubble-front and spike positions for RTI. (a) At $t^* = 0.5$ and $Re = 256$; (b) At $t^* = 0.5$ and $Re = 3000$; and (c) At $t^* = 0.998$ and $Re = 3000$.

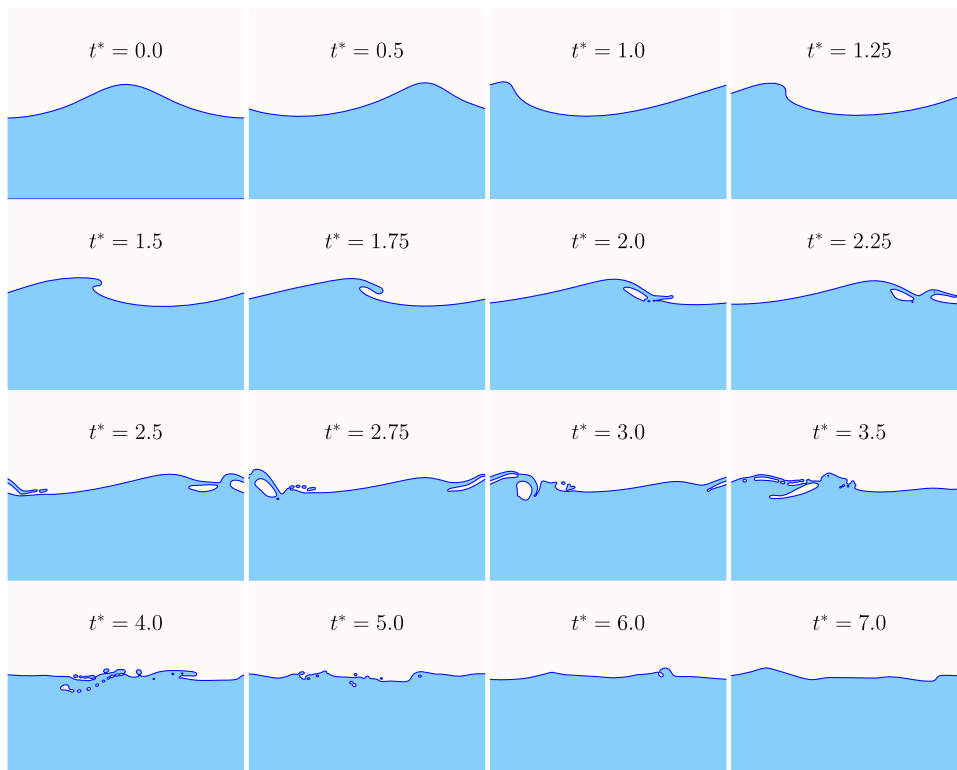


FIG. 11. Snapshots of the time sequence of a plunging breaking wave.

instant when the maximum horizontal velocity is observed. The time instant t is normalized by the wave period T_C , $t_T = t/T_C$ and the velocity by phase speed, $\max(U_x^*) = \max(U_x)/C$. The $\max(U_x^*)$ is found when the splash-up mechanism is about to begin, and its magnitude is 2.16 times the phase speed, whereas Chen *et al.*⁴⁶ reported the magnitude of 2.39. This maximum velocity is located at the tip of

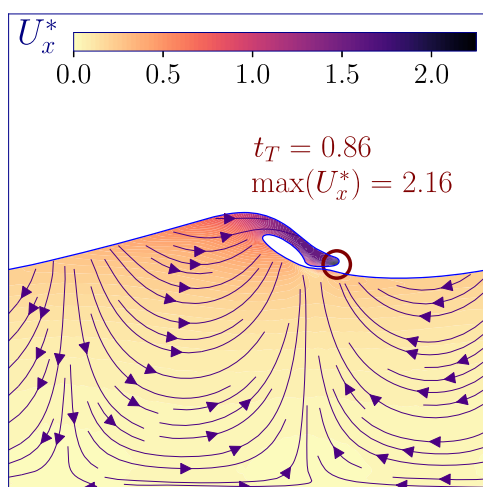


FIG. 12. Stream lines and velocity contours at the time instant of maximum velocity.

the splash emerging from the plunge-point (Fig. 12). Since $\max(U_x^*)$ exceeds the phase velocity, the present breaking wave simulation obeys the kinematic breaking criterion.

The wave breaking is a result of its instability leading to the loss of its energy content. For different wave characteristics, the quantification of energy loss is made only through wave height measurements obtained from field observations or experiments. On the other hand, numerical simulations provide a detailed knowledge of both the velocity field and the surface elevation, which in-turn, provide the direct estimates of energy as well as the detailed description of the breaking process. The total mechanical energy (TE) composed of potential energy (PE) and kinetic energy (KE), which are calculated based on Refs. 46, 47, and 49 and are normalized by the respective initial values. The comparison of normalized PE, KE, and TE with that of Chen *et al.*⁴⁶ and Wang *et al.*⁴⁹ is given in Fig. 13. The difference in higher KE at the initial stages between Refs. 46 and 49 is attributed to the difference in the grid size adopted. Since the grid size in the present study is the same as that of Ref. 46, no significant variation has been observed at the initial stages up to $t^* < 1.5$. In the work of Chen *et al.*,⁴⁶ the density and viscosity ratios are 100 and 2.5, respectively. However, in the present study, these ratios are similar to the air-water system. Even though the Re and Bo were the same, the differences in the fluid properties yield a higher estimate of energies, which are observed after $t^* > 1.5$. The comparison of energies reveals that the overall trend is in agreement with the results of direct numerical simulation (DNS) solution of Ref. 46 and the high fidelity solution of Ref. 49 using the NS-VoF solvers. According to Chen *et al.*,⁴⁶ the total energy decay takes the exponential form, $\exp(-2\zeta t)$

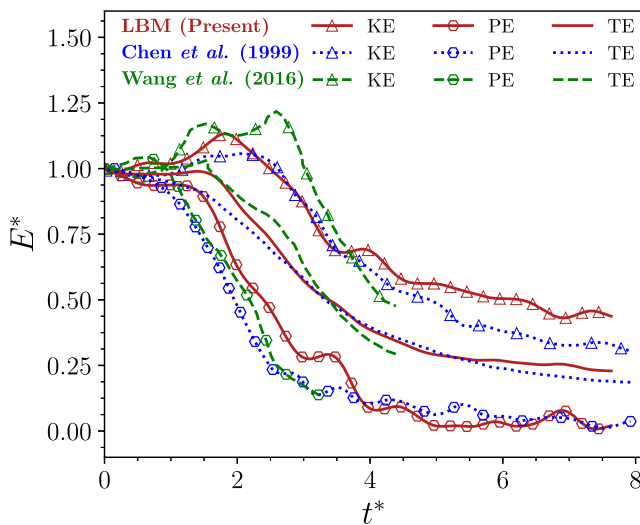


FIG. 13. Comparison of normalized potential, kinetic, and total energies with the numerical solutions from Refs. 46 and 49.

until the two wave periods after the time of breaking, and then the decay follows the algebraic form. During breaking, i.e., $1.5 < t^* < 5.2$, the rate of decay ζ was estimated to be 0.16. In the present study $\zeta = 0.17$, but the duration of breaking becomes shorter, i.e., $1.5 < t^* < 4.6$. After the breaking process $t^* > 8$, the remaining potential energy is around 5%, which is the same as that of Chen *et al.*⁴⁶ however, the remaining kinetic energy is of 44% compared to 30% in Chen *et al.*⁴⁶ This increased KE results in the loss of only 75% of the total prebreaking energy compared to the loss of 80% reported by Chen *et al.*⁴⁶

IV. SUMMARY AND CONCLUSIONS

In the present study, the LB model suitable for two phase flows involving air and water has been developed. The present model employs the normalized pressure evolution based LB model⁹ for the flow field and the conservative Allen-Cahn LB model³⁰ for the interface along with an additional interfacial force term³¹ to ensure incompressibility at the interface. Numerical results obtained from the stationary drop and bubble coalescence test show that the model obeys the mass conservation law. The results of the capillary wave test exhibit the dependence of angular frequency on grid size and wave elevation on the chosen viscosity. Satisfactory agreement with the experimental measurements has been obtained for the case of air bubble rising in water. The emergence of multiple secondary droplets when the drop impacts upon a wet bed for $Re \geq 500$ shows the model suitability for further study on droplet impact. The Rayleigh-Taylor instability simulation shows good agreement with previous results on the evolution of spike/bubble front and proves the model's capability in handling complex topological changes involved in the flow. Breaking of deep water waves is simulated for high Re $O(10^4)$ regimes, and the result shows that the model can handle high Re flows and large density ratio of fluids simultaneously. The observed plunging breaker has lost nearly 75% of the prebreaking wave energy. Prior to breaking, the maximum crest velocity has

exceeded the phase speed, which is in accordance with the kinematic breaking criterion. Thus, the application of the present LB model can be further explored for different complex scenarios of wave breaking and, in particular, breaking of capillary-gravity waves.

REFERENCES

- A. Babanin, *Breaking and Dissipation of Ocean Surface Waves* (Cambridge University Press, 2011).
- G. Tryggvason, B. Bunner, A. Esmaeeli, D. Juric, N. Al-Rawahi, W. Tauber, J. Han, S. Nas, and Y.-J. Jan, "A front-tracking method for the computations of multiphase flow," *J. Comput. Phys.* **169**, 708–759 (2001).
- C. W. Hirt and B. D. Nichols, "Volume of fluid (VOF) method for the dynamics of free boundaries," *J. Comput. Phys.* **39**, 201–225 (1981).
- S. Osher and R. Fedkiw, *Level Set Methods and Dynamic Implicit Surfaces* (Springer Science & Business Media, New York, 2006), Vol. 153.
- C. Körner, M. Thies, T. Hofmann, N. Thürey, and U. Rude, "Lattice Boltzmann model for free surface flow for modeling foaming," *J. Stat. Phys.* **121**, 179–196 (2005).
- C. F. Janßen, S. T. Grilli, and M. Krafczyk, "On enhanced non-linear free surface flow simulations with a hybrid LBM-VOF model," *Comput. Math. Appl.* **65**, 211–229 (2013).
- X. He, S. Chen, and R. Zhang, "A lattice Boltzmann scheme for incompressible multiphase flow and its application in simulation of Rayleigh–Taylor instability," *J. Comput. Phys.* **152**, 642–663 (1999).
- H. Liang, B. C. Shi, Z. L. Guo, and Z. H. Chai, "Phase-field-based multiple-relaxation-time lattice Boltzmann model for incompressible multiphase flows," *Phys. Rev. E* **89**, 053320 (2014).
- A. Fakhari, T. Mitchell, C. Leonardi, and D. Bolster, "Improved locality of the phase-field lattice-Boltzmann model for immiscible fluids at high density ratios," *Phys. Rev. E* **96**, 053301 (2017).
- T. Lee and L. Liu, "Lattice Boltzmann simulations of micron-scale drop impact on dry surfaces," *J. Comput. Phys.* **229**, 8045–8063 (2010).
- Q. Lou, Z. Guo, and B. Shi, "Effects of force discretization on mass conservation in lattice Boltzmann equation for two-phase flows," *EPL* **99**, 64005 (2012).
- F. Qin, A. M. Moqaddam, Q. Kang, D. Derome, and J. Carmeliet, "Entropic multiple-relaxation-time multirange pseudopotential lattice Boltzmann model for two-phase flow," *Phys. Fluids* **30**, 032104 (2018).
- L. Fei, J. Du, K. H. Luo, S. Succi, M. Lauricella, A. Montessori, and Q. Wang, "Modeling realistic multiphase flows using a non-orthogonal multiple-relaxation-time lattice Boltzmann method," *Phys. Fluids* **31**, 042105 (2019).
- J. Y. Shao, C. Shu, H. B. Huang, and Y. T. Chew, "Free-energy-based lattice Boltzmann model for the simulation of multiphase flows with density contrast," *Phys. Rev. E* **89**, 033309 (2014).
- M. A. Safi and S. Turek, "GPGPU-based rising bubble simulations using a MRT lattice Boltzmann method coupled with level set interface capturing," *Comput. Fluids* **124**, 170–184 (2016).
- Y. Wang, C. Shu, and L. Yang, "An improved multiphase lattice Boltzmann flux solver for three-dimensional flows with large density ratio and high Reynolds number," *J. Comput. Phys.* **302**, 41–58 (2015).
- D. Lycett-Brown and K. H. Luo, "Improved forcing scheme in pseudopotential lattice Boltzmann methods for multiphase flow at arbitrarily high density ratios," *Phys. Rev. E* **91**, 023305 (2015).
- A. Banari, C. F. Janßen, and S. T. Grilli, "An efficient lattice Boltzmann multiphase model for 3D flows with large density ratios at high Reynolds numbers," *Comput. Math. Appl.* **68**, 1819–1843 (2014).
- T. Inamuro, T. Ogata, S. Tajima, and N. Konishi, "A lattice Boltzmann method for incompressible two-phase flows with large density differences," *J. Comput. Phys.* **198**, 628–644 (2004).
- Y. Q. Zu and S. He, "Phase-field-based lattice Boltzmann model for incompressible binary fluid systems with density and viscosity contrasts," *Phys. Rev. E* **87**, 043301 (2013).
- A. K. Gunstensen, D. H. Rothman, S. Zaleski, and G. Zanetti, "Lattice Boltzmann model of immiscible fluids," *Phys. Rev. A* **43**, 4320 (1991).

- ²²X. Shan and H. Chen, "Lattice Boltzmann model for simulating flows with multiple phases and components," *Phys. Rev. E* **47**, 1815 (1993).
- ²³M. R. Swift, E. Orlandini, W. Osborn, and J. Yeomans, "Lattice Boltzmann simulations of liquid-gas and binary fluid systems," *Phys. Rev. E* **54**, 5041 (1996).
- ²⁴P. Lallemand, L.-S. Luo, and Y. Peng, "A lattice Boltzmann front-tracking method for interface dynamics with surface tension in two dimensions," *J. Comput. Phys.* **226**, 1367–1384 (2007).
- ²⁵H.-Z. Yuan, C. Shu, Y. Wang, and S. Shu, "A simple mass-conserved level set method for simulation of multiphase flows," *Phys. Fluids* **30**, 040908 (2018).
- ²⁶J. Y. Shao and C. Shu, "A hybrid phase field multiple relaxation time lattice Boltzmann method for the incompressible multiphase flow with large density contrast," *Int. J. Numer. Methods Fluids* **77**, 526–543 (2015).
- ²⁷Y. Wang, C. Shu, H. Huang, and C. Teo, "Multiphase lattice Boltzmann flux solver for incompressible multiphase flows with large density ratio," *J. Comput. Phys.* **280**, 404–423 (2015).
- ²⁸T. Lee and C.-L. Lin, "A stable discretization of the lattice Boltzmann equation for simulation of incompressible two-phase flows at high density ratio," *J. Comput. Phys.* **206**, 16 (2005).
- ²⁹M. Geier, A. Fakhari, and T. Lee, "Conservative phase-field lattice Boltzmann model for interface tracking equation," *Phys. Rev. E* **91**, 063309 (2015).
- ³⁰F. Ren, B. Song, M. C. Sukop, and H. Hu, "Improved lattice Boltzmann modeling of binary flow based on the conservative Allen-Cahn equation," *Phys. Rev. E* **94**, 023311 (2016).
- ³¹Q. Li, K. Luo, Y. Gao, and Y. He, "Additional interfacial force in lattice Boltzmann models for incompressible multiphase flows," *Phys. Rev. E* **85**, 026704 (2012).
- ³²M. Krafczyk, J. Tölke, and L.-S. Luo, "Large-eddy simulations with a multiple-relaxation-time LBE model," *Int. J. Mod. Phys. B* **17**, 33–39 (2003).
- ³³P. M. Dupuy, M. Fernandino, H. A. Jakobsen, and H. F. Svendsen, "Fractional step two-phase flow lattice Boltzmann model implementation," *J. Stat. Mech.: Theory Exp.* **2009**, P06014.
- ³⁴C. Shu, X. Niu, Y. Chew, and Q. Cai, "A fractional step lattice Boltzmann method for simulating high Reynolds number flows," *Math. Comput. Simul.* **72**, 201–205 (2006).
- ³⁵L. L. Wollk *et al.*, TCLB -templated mpi+cuda/cpu lattice Boltzmann code, <https://github.com/CFD-GO/TCLB>.
- ³⁶L. L. Wollk and J. Rokicki, "Adjoint lattice Boltzmann for topology optimization on multi-GPU architecture," *Comput. Math. Appl.* **71**, 833–848 (2016).
- ³⁷H. Zheng, C. Shu, and Y. Chew, "A lattice Boltzmann model for multiphase flows with large density ratio," *J. Comput. Phys.* **218**, 353–371 (2006).
- ³⁸A. Prosperetti, "Motion of two superposed viscous fluids," *Phys. Fluids* **24**, 1217–1223 (1981).
- ³⁹R. Clift, J. R. Grace, and M. E. Weber, *Bubbles, Drops, and Particles* (Courier Corporation, 2005).
- ⁴⁰D. Bhaga and M. E. Weber, "Bubbles in viscous liquids: Shapes, wakes and velocities," *J. Fluid Mech.* **105**, 61 (1981).
- ⁴¹J. Hua, J. F. Stene, and P. Lin, "Numerical simulation of 3D bubbles rising in viscous liquids using a front tracking method," *J. Comput. Phys.* **227**, 3358–3382 (2008).
- ⁴²H. Huang, J.-J. Huang, and X.-Y. Lu, "A mass-conserving axisymmetric multiphase lattice Boltzmann method and its application in simulation of bubble rising," *J. Comput. Phys.* **269**, 386–402 (2014).
- ⁴³L. Amaya-Bower and T. Lee, "Single bubble rising dynamics for moderate Reynolds number using lattice Boltzmann method," *Comput. Fluids* **39**, 1191–1207 (2010).
- ⁴⁴Z. Chen, C. Shu, D. Tan, X. D. Niu, and Q. Z. Li, "Simplified multiphase lattice Boltzmann method for simulating multiphase flows with large density ratios and complex interfaces," *Phys. Rev. E* **98**, 063314 (2018).
- ⁴⁵C. Josserand and S. Zaleski, "Droplet splashing on a thin liquid film," *Phys. Fluids* **15**, 1650–1657 (2003).
- ⁴⁶G. Chen, C. Kharif, S. Zaleski, and J. Li, "Two-dimensional Navier–Stokes simulation of breaking waves," *Phys. Fluids* **11**, 121–133 (1999).
- ⁴⁷A. Iafrati, "Energy dissipation mechanisms in wave breaking processes: Spilling and highly aerated plunging breaking events," *J. Geophys. Res.* **116**, C07024, <https://doi.org/10.1029/2011jc007038> (2011).
- ⁴⁸A. Iafrati, "Numerical study of the effects of the breaking intensity on wave breaking flows," *J. Fluid Mech.* **622**, 371–411 (2009).
- ⁴⁹Z. Wang, J. Yang, and F. Stern, "High-fidelity simulations of bubble, droplet and spray formation in breaking waves," *J. Fluid Mech.* **792**, 307–327 (2016).
- ⁵⁰M. Brocchini and D. H. Peregrine, "The dynamics of strong turbulence at free surfaces. Part 1. Description," *J. Fluid Mech.* **449**, 225 (2001).
- ⁵¹C. Song and A. I. Sirviente, "A numerical study of breaking waves," *Phys. Fluids* **16**, 2649–2667 (2004).
- ⁵²L. Deike, S. Popinet, and W. Melville, "Capillary effects on wave breaking," *J. Fluid Mech.* **769**, 541–569 (2015).
- ⁵³J. Chao, R. Mei, R. Singh, and W. Shyy, "A filter-based, mass-conserving lattice Boltzmann method for immiscible multiphase flows," *Int. J. Numer. Methods Fluids* **66**, 622–647 (2011).